



CHORUS

This is the accepted manuscript made available via CHORUS. The article has been published as:

Polyamorphic transitions in Ce-based metallic glasses by synchrotron radiation

M. J. Duarte, P. Bruna, E. Pineda, D. Crespo, G. Garbarino, R. Verbeni, K. Zhao, W. H. Wang, A. H. Romero, and J. Serrano

Phys. Rev. B **84**, 224116 — Published 22 December 2011

DOI: [10.1103/PhysRevB.84.224116](https://doi.org/10.1103/PhysRevB.84.224116)

Polyamorphic transitions in Ce-based metallic glasses by synchrotron radiation

M. J. Duarte,^{1,2} P. Bruna,¹ E. Pineda,¹ D. Crespo,¹ G. Garbarino,³ R. Verbeni,³ K. Zhao,⁴ W. H. Wang,⁴ A. H. Romero,² and J. Serrano⁵

¹*Departament de Física Aplicada, EPSC, Universitat Politècnica de Catalunya, C. Esteve Terradas 15, E-08860 Castelldefels, Spain*

²*Departamento de Materiales, CINVESTAV-Unidad Querétaro, Libramiento Norponiente 2000, 76230 Querétaro, Mexico*

³*European Synchrotron Radiation Facility, B.P. 220, 38043 Grenoble Cedex 9, France*

⁴*Institute of Physics, Chinese Academy of Sciences, 100080 Beijing, PR China*

⁵*ICREA - Departament de Física Aplicada, EPSC, Universitat Politècnica de Catalunya, C. Esteve Terradas 15, E-08860 Castelldefels, Spain*

We report here a polyamorphic phase transition upon application of pressure on a Ce-based metallic glass (MG), $\text{Ce}_{70}\text{Al}_{10}\text{Ni}_{10}\text{Cu}_{10}$, investigated by X-ray diffraction (XRD) and inelastic X-ray scattering (IXS). This alloy is found to display a strong hysteresis in the volume per atom upon application and subsequent release of pressure. The observed structural changes are correlated with changes observed by IXS in the elastic constants, acoustic mode frequencies and sound speed. The results reported here point towards three different amorphous phases for this alloy existing in the 0 - 25 GPa pressure region: a low and a high density states and an intermediate mixed state that displays a hysteresis behavior. Finally, we discuss the impact of Ce concentration on the polyamorphic transition for a series of Ce-based metallic glasses alloys and link it to the phase transformation between γ -Ce and α -Ce under pressure.

PACS numbers: 62.50.-p, 63.50.Lm, 64.70.kj, 81.30.Hd

I. INTRODUCTION

Phase transitions in single crystals are known since the first applications of high pressure research in the fifties. The study of similar transitions in liquids and amorphous solids, however, has been undertaken much later due to the limited structural information available via X-ray and neutron diffraction techniques. The evidence of a transition in amorphous ice when compressed at 77 K from a low-density state to a high-density amorphous ice at 0.6 GPa¹ changed the point of view concerning to polyamorphism. Such transitions have been observed, for example, in liquid phosphorous² and sulfur,³ by X-ray diffraction and neutron diffraction techniques respectively, regarding for static signatures. Other examples of this phenomena include Si,⁴⁻⁶ binary liquids such as $\text{Y}_2\text{O}_3\text{-Al}_2\text{O}_3$,^{7,8} vitreous SiO_2 ,^{9,10} and GeAsS chalcogenide glasses.¹¹

More recently, metallic glasses (MGs) have attracted interest as a new class of amorphous materials due to their potential for structural applications.¹² The mixture of metallic binding with partial covalent bonds created by non-metals such as boron, carbon, silicon, and phosphorous makes the study of polyamorphic transitions in MGs very appealing as a source of information about the role of the electronic structure on the transition.

Recently, polyamorphic transitions have been evidenced in nondirectional, densely-packed metallic glasses.¹³ Using a combination of XRD experiments and theoretical calculations, a polyamorphic transition upon application of pressure was found in $\text{Ce}_{55}\text{Al}_{45}$ metallic glass in the 2–13.5 GPa range. XRD patterns showed hysteresis in the pressure dependence of the specific volume upon compression and decompression, with 14%

density difference between the two amorphous states of the metallic glass at ambient pressure. Those results were compared with *ab-initio* calculations and discussed in terms of a pressure-driven change in the localization of $4f$ Ce electronic states, similar to the behavior observed in the γ - α phase transformation in crystalline cerium.^{14,15} A similar case was latter reported in $\text{Ce}_{75}\text{Al}_{25}$ metallic glass.¹⁶

The entanglement of structural polyamorphism with the specific electronic properties of Cerium makes the case for the recent research efforts devoted to investigate Ce-based MGs under pressure. Despite the extant evidences of structural changes and the role of $4f$ Ce electrons reported for these alloys, essential questions still remain unanswered, such as how these polyamorphism phenomena affect other material properties and to which extent the Ce-content and its peculiar electronic behavior upon application of pressure drive the polyamorphic transition, namely volume collapse, transition pressure, and other parameters. Only recently, Zeng et.al. reported a clear change in thermodynamic and electronic transport properties of $\text{Ce}_{75}\text{Al}_{25}$ as a result of the transition at 1.5 GPa.¹⁷ The electronic delocalization may be anticipated to certainly affect Ce-based MGs mechanical properties, however, no direct observation has been achieved so far, partly due to the challenge of using traditional ultrasonic methods to reach the required high pressures. Inelastic x-ray scattering (IXS) provides a unique access to this pressure range and, coupled with high resolution X-ray diffraction (XRD), allows one to shed light on the correlations between structural and mechanical changes.

We present here pressure dependent studies of struc-

tural and mechanical properties of $\text{Ce}_{70}\text{Al}_{10}\text{Ni}_{10}\text{Cu}_{10}$ metallic glass. $\text{Ce}_{70}\text{Al}_{10}\text{Ni}_{10}\text{Cu}_{10}$ can be produced in completely glassy state with a critical diameter of 3 mm,¹⁸ and it is then the first bulk metallic glass (BMG) reported with polyamorphism. X-ray diffraction and inelastic X-ray scattering experiments using synchrotron radiation were carried out accounting for static and dynamic signatures of the MG, respectively. We find three different amorphous regions in the 0–25 GPa pressure range and a different behavior upon application of pressure and decompression. For the chosen alloy, acoustic and elastic properties as function of pressure up to 0.5 GPa reported previously show a unusual behavior compared with other MGs.¹⁹ Our IXS results agree with this behavior and allow one to understand the consequences of the polyamorphic transition in the mechanical properties, i.e. longitudinal sound speed and elastic constant, up to 25 GPa, thus covering the full transition between the low and high density states. We discuss as well the role of the Cerium content in the polyamorphic transition by a thorough analysis of the extant XRD data reported in the literature.

II. EXPERIMENTAL METHODS

The samples for both XRD and IXS experiments were cut from melt spun ribbons stemming from a 4 mm diameter rod of $\text{Ce}_{70}\text{Al}_{10}\text{Ni}_{10}\text{Cu}_{10}$ produced by mold cast. All experiments were conducted at room temperature on the same batch of ribbons, thus ensuring the reliability and allowing for a direct comparison of structural and mechanical properties. They were loaded into diamond anvil cells (DAC) together with ruby pieces to calibrate and measure pressure using the ruby fluorescence levels.^{20,21}

XRD experiments were conducted in beamline ID27 at the European Synchrotron Radiation Facility (ESRF). Incident energy of 33 keV was focused on the sample by using the highly focalized micrometric sized X-ray beam available at ID27 ($3 \times 2 \mu\text{m}^2$). Small pieces of about 60 μm diameter and 30–50 μm thick were cut from the ribbons and inserted in the DAC for pressure application. Liquid Helium was loaded in the DAC as pressure transmitting medium. XRD patterns were acquired in the 0–25 GPa pressure range upon both compression and decompression ramps in transmission mode through the diamonds. In the proximity of the sample, a diffraction pattern of the DAC solely was recorded at each pressure point. These spectra were used as background and subtracted to the sample signals after intensity normalization.

The IXS experiment was performed in beamline ID28 at the ESRF. The instrument was operated using the Si 999 Bragg reflection of the main monochromator, with an incident energy of 17.794 keV. This configuration yields a momentum transfer resolution of 0.27 nm^{-1} and energy transfer resolution of 3 meV. IXS energy scans were performed in the range of -25 to 25 meV with an energy

step of 0.5 meV for momentum transfers between 2 and 12 nm^{-1} . Spectra corresponding to eight different momentum transfers were recorded simultaneously using a multi-analyzer setup. In order to optimize the IXS signal, 30–50 μm thick ribbons were selected and two samples of 170×150 and $95 \times 95 \mu\text{m}^2$ were cut and mounted on DACs. Liquid Neon and Helium were loaded in the DACs together with the first and second samples, respectively, as pressure transmitting mediums. The largest sample was used to obtain data up to 12.5 GPa, pressure at which the DAC failed. The second sample was employed to obtain higher pressure data and the data upon decompression. Both data sets display a similar behavior at low pressure, which ensure the reliability and the hydrostatic conditions obtained with both pressure transmitting media.

III. RESULTS AND DISCUSSION

A. Structural properties

Figure 1 shows integrated XRD patterns obtained in beamline ID27 in the 0 to 25 GPa pressure range, upon both compression and decompression. The lower panels display intensity plots to highlight the spectral weight redistribution in momentum transfer as a function of pressure. The samples remain amorphous in the whole pressure range, showing no signs of crystallization. A main peak is observed at 22.6 nm^{-1} , followed by broader features at 38.2 and 55.2 nm^{-1} . Upon compression, the main peak shifts to higher momentum transfer, displaying a distinct behavior at the lowest pressures: Below nearly 3 GPa, the peak shift occurs faster than at higher pressures, thus indicating the possible onset of the first amorphous–amorphous transformation. This shift is accompanied with a redistribution of the spectral weight corresponding to the second diffraction peak: it broadens and at pressures larger than 2 GPa a satellite structure appears at 50 nm^{-1} . This redistribution is more apparent in the lower panels. At higher pressure, the satellite also shifts to higher Q values with increasing pressure, and both features decrease in relative intensity with respect to the main peak. Upon decompression, the same change in the intensity distribution is apparent at pressures lower than 4 GPa, and a sudden shift to lower momentum transfer of the main peak is observed below 2 GPa. The XRD patterns thus seem to reveal 3 distinct density regions, corresponding to the 0–2 GPa, 2–10 GPa and higher pressure ranges, pointing to the presence of phase transformations between amorphous structures for $\text{Ce}_{70}\text{Al}_{10}\text{Ni}_{10}\text{Cu}_{10}$. The approximate values where the transition occurs are more evident when the volume change is plotted as seen in the inset of Fig. 2.

Figure 2 displays the specific volume as a function of pressure for both compression and decompression processes. The volume ratio was determined using the values of the momentum transfer at the main diffraction

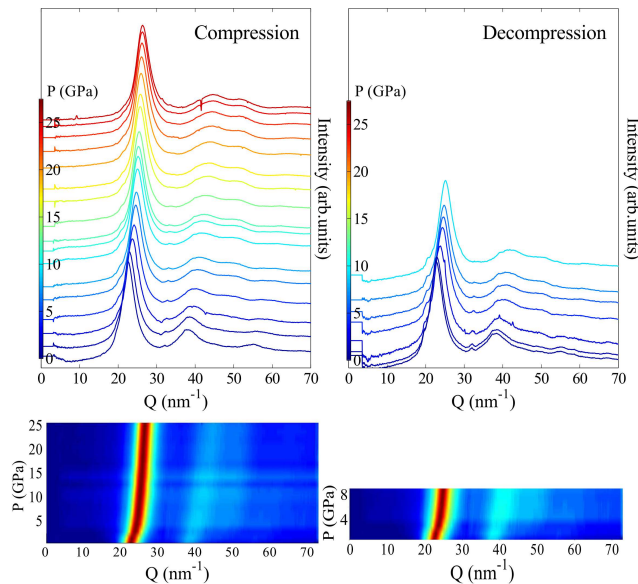


FIG. 1: (color on-line) XRD integrated intensity patterns of $\text{Ce}_{70}\text{Al}_{10}\text{Ni}_{10}\text{Cu}_{10}$ metallic glass obtained during compression and decompression. The lower panels display the intensity plot normalized to the intensity of the main diffraction peak, in order to highlight the spectral weight redistribution.

peak observed in Fig. 1 and the specific volume estimated for the $\text{Ce}_{70}\text{Al}_{10}\text{Ni}_{10}\text{Cu}_{10}$ alloy at ambient pressure and temperature. Solid and open symbols correspond to data obtained during compression and decompression, respectively.

Upon application of pressure, two distinct regimes are clearly observed: The upper black dashed line at low pressure displays the equation of state (EOS) calculated from results up to 0.5 GPa reported by B. Zhang et al.¹⁹, thus showing a reasonable agreement with our low pressure data. Specific volume decreases faster between 0 to 4 GPa in agreement with the shift in the main peak of the structure factor evidenced in Fig. 1. At pressures larger than 10 GPa, the specific volume displays a pressure dependence that can be fitted to a general Murnaghan²² type EOS (lower green dashed line). The latter fit was actually performed taking into account only pressure points above 15 GPa. These two regimes represent hence the low and high density states.

Between 4 and 10 GPa, the specific volume displays a non-linear pressure dependence. Note the different convexity displayed by both EOS, which point out to either an anomalous pressure dependence of the specific volume or to the existence of a third region where the convexity gradually changes. The latter might be the underlying reason for the hysteresis evidenced between compression and decompression processes. In order to ascertain more clearly the pressure range of this mixed density region, we plot in the inset of Fig. 2 the change in specific volume between compression and decompression, as function of pressure. To obtain this figure, spline

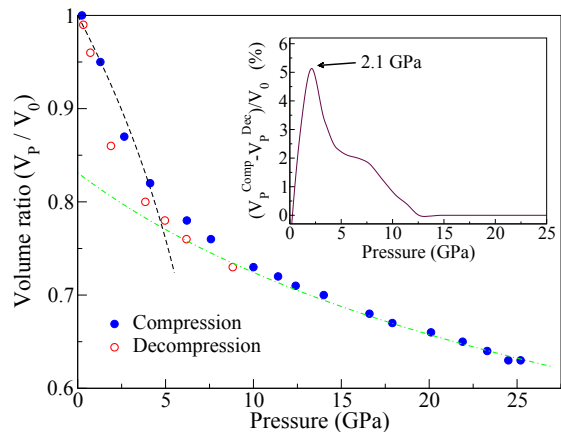


FIG. 2: Relative specific volume versus pressure. Solid and open symbols correspond to data taken during compression and decompression, respectively. Dashed lines represent estimated EOS drawn as guides-to-the-eyes to highlight the low (black) and high (green) density states observed at ambient and high pressure, respectively. The EOS corresponding to the low density state, upper black dashed line, was obtained from data up to 0.5 GPa reported in Ref. 19. The inset shows the pressure dependence of the hysteresis by displaying the difference in volume ratio upon compression and decompression as a function of pressure.

interpolation curves of both up-load and down-load specific volume data sets were subtracted. The data set for decompression was completed with those pressure points taken at pressures higher than 15 GPa, i.e. the high pressure limit. This inset shows a peak change in volume ratio at nearly 2 GPa, with a maximum difference in volume ratio of nearly 5.5%, followed with a decrease in hysteresis up to 12 GPa. Despite the wiggles due to the reduced number of data points, an abrupt change in hysteresis is observed at 2 GPa, which make us assign this pressure value to the onset of the intermediate density region.

Hence, these results suggest that the $\text{Ce}_{70}\text{Al}_{10}\text{Ni}_{10}\text{Cu}_{10}$ metallic glass exhibits three different amorphous regions upon application of pressure. A low-density state is observed at ambient conditions which becomes a higher-density state while increasing pressure, with an intermediate region that shows a gradual transition linking both density states and displays hysteresis through compression and decompression stages. Between both density states there is a volume collapse of $\sim 16\%$ extrapolated at ambient pressure. This hysteresis cycle and large volume collapse are in agreement with previous works^{13,14,23} where the transition was assigned to be carried out by means of pressure induced delocalization of Ce 4*f* electrons. A similar behavior was reported for $\text{Ce}_{75}\text{Al}_{25}$ MG where an 8.6% volume collapse was observed at the same pressure as a transformation of Ce 4*f* electrons from a localized state at ambient pressure to an itinerant state

at high pressure.¹⁶ The origin of this polyamorphism can be attributed to a similar electronic transformation observed in crystalline Cerium accompanying a phase transformation between γ -Ce and α -Ce, at 0.9 GPa.^{14,15} We will resume this point later in the discussion.

B. Mechanical properties

Given the large electron-phonon coupling in Ce and the substantial amount of this element in the alloy,^{24,25} changes in the electronic band structure should be followed by changes in the phonon dispersion relations and sound velocities.

High pressure IXS experiments were performed to unveil the effect of the polyamorphic transition on the mechanical properties of Ce-based alloys at a microscopic level. In order to cover the full pressure range up to a complete transition, IXS spectra were acquired from 0 to 22 GPa upon increase of pressure, and then at 10 GPa upon pressure decrease.

Figure 3(a) displays representative IXS spectra for the eight values of the momentum transfer obtained simultaneously at 0.4 GPa. The spectra consist in a central elastic peak at zero energy transfer followed by additional peaks at positive and negative energies that correspond to longitudinal acoustic excitations of $\text{Ce}_{70}\text{Al}_{10}\text{Ni}_{10}\text{Cu}_{10}$ metallic glass. The elastic peak has been truncated in order to enhance the features corresponding to the acoustic waves.

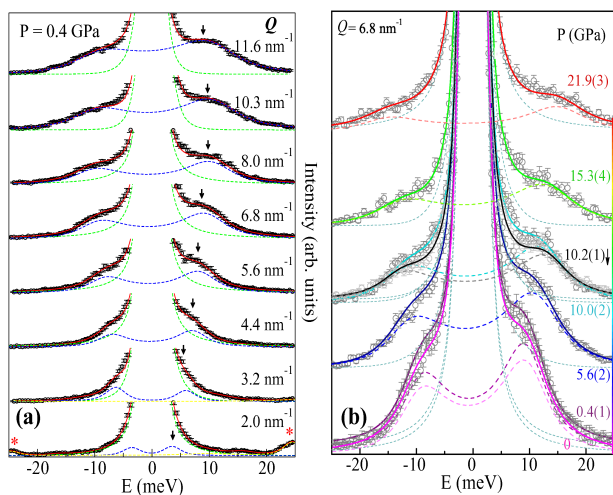


FIG. 3: (Color on-line) Selected IXS spectra of the $\text{Ce}_{70}\text{Al}_{10}\text{Ni}_{10}\text{Cu}_{10}$ metallic glass for: (a) 0.4 GPa and Q between 2 and 12 nm^{-1} , and (b) $Q = 6.8 \text{ nm}^{-1}$ and pressures up to 22 GPa. Open circles correspond to experimental data and solid lines to the best fit obtained using Eq.1. The individual components of the excitation and elastic line are displayed with dashed lines.

The IXS spectra is proportional to the dynamic structure factor, $S(Q, \omega)$, and can be fitted using as model

function a damped harmonic oscillator for each excitation and a delta function for the elastic line, convoluted both with the experimental resolution function²⁶

$$\frac{S(Q, \omega)}{S(Q)} = A(Q)\delta(\omega) + \frac{1 - A(Q)}{\pi} \times \frac{\Omega^2(Q)\Gamma(Q)}{[\omega^2 - \Omega^2(Q)]^2 + \omega^2\Gamma^2(Q)} \quad (1)$$

where, at a given momentum transfer Q , $S(Q)$ is the static structure factor measured using standard x-ray diffraction, $A(Q)$ is the intensity of the elastic scattering relative to the spectrum total intensity, $\Omega(Q)$ is the characteristic frequency of the acoustic mode and corresponds to the maximum of the longitudinal current spectra $C_L(Q, \omega) = (\omega/Q)^2 S(Q, \omega)$, and $\Gamma(Q)$, denoted as phonon damping, is a parameter related to the sound attenuation and the full-width-at-half-maximum (FWHM) of the excitation signal.²⁶ Dashed lines represent the elastic (green) and inelastic (blue) contributions derived from the model after convolution to the experimental instrumental function, which is analyzer-dependent. At the lowest momentum transfer, a transverse acoustic phonon of diamond from the anvil cell appears and is marked with a red asterisk. Due to the higher sound speed of this mode, 11 km/s, it goes out of the region-of-interest with increasing momentum transfer.

The broadening of acoustic excitations with increasing momentum transfer indicates an increase in the sound attenuation, up a point where the broadening becomes so large that it is no longer valid the term of propagating excitations to refer to the modes.²⁷

The energy of these acoustic-like excitations has a typical behavior of acoustic modes: it firstly increases with the increasing momentum transfer at low Q values and then starts to decrease when the highest Q values are reached, as displayed by the arrows in Fig. 3(a). The excitation intensity increases as well with Q , due to both the increase of broadening and energy.

Figure 3(b) shows selected IXS spectra corresponding to a momentum transfer of 6.8 nm^{-1} upon compression up to 22 GPa, and at 10.2 GPa in decompression. With increasing pressure, a blue-shift of the excitation energy occurs. This corresponds to a stiffening of the amorphous medium upon application of pressure, similarly to what is observed in their crystalline counterpart. The energy of the excitations increases while increasing pressure following an almost linear relation. On the other hand the intensity decreases when higher pressure is applied, which might be attributed to changes in the pressure transmitting medium.

A close-up on the IXS curves during compression and decompression at $Q = 6.8 \text{ nm}^{-1}$ is presented in Fig. 4. The lower intensity of the excitation during decompression suggests an hysteresis effect on the mechanical properties of the $\text{Ce}_{70}\text{Al}_{10}\text{Ni}_{10}\text{Cu}_{10}$ metallic glass going upwards and downwards the structural polyamorphic transition. This hysteresis is further emphasized by the 0.5 meV energy increase observed at the excitation energy

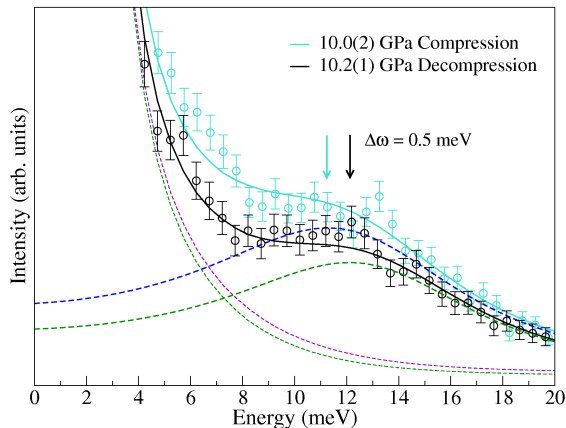


FIG. 4: Example of the different behavior of the IXS intensity band shift during compression and decompression at around 10 GPa and 6.8 nm^{-1} .

from compression to decompression. At lower momentum transfers, the IXS spectra taken during the pressure increase and decrease processes almost retrace on each other and the energy shift becomes negligible. At 11.6 nm^{-1} , however, the energy shift becomes more than double, thus evidencing that the hysteresis in structural properties also create an hysteresis in the mechanical properties.

Similarly to what happens in single crystals, at a given pressure, the dependence of the acoustic excitation energy on momentum transfer can be plotted in a diagram and follows a dispersing curve, the so-called longitudinal acoustic dispersion relation for the amorphous material. The dispersion relation has an almost linear dependence on Q when Q tends to zero and its slope at this limit corresponds to the macroscopic longitudinal sound velocity.²⁸ Figure 5(a) displays such dispersion curves obtained at different pressures from the excitation energies shown in the previous figures. The dispersion curves behave like a typical sinusoidal function that peaks at momentum transfers between 10 and 12 nm^{-1} , depending on the applied pressure. This maximum turns out to be at the same momentum transfer Q_{max} as half that of the main peak of the static structure factor determined with XRD, which allows one to understand the amorphous material as presenting a pseudo-Brillouin zone of characteristic length equal to $2Q_{max}$. Note the different value of Q_{max} observed at 10 GPa for pressure increasing and decreasing processes. This again reflects the structural hysteresis observed in the polyamorphic transition. An anomalous behavior is observed at low pressures where a softening of the longitudinal acoustic mode upon increase of pressure between 0 and 0.4 GPa is clearly evidenced in Fig. 5(a).

The longitudinal sound velocity was obtained by extrapolating a sinusoidal fit of the dispersion relations to zero momentum transfer and taking the slope at this limit

for each pressure. The calculated velocities are displayed in Fig. 5(b). By following this procedure, a longitudinal sound speed of 2.78 km/s is obtained at ambient pressure. Different symbols are used to represent data stemming from different samples upon compression and decompression. A pressure induced decrease in sound velocity of $\sim 1.4\%$ is observed at low pressure. This decrease correlates with the softening of the mode observed in Fig. 5(a).

It is worthwhile to notice that a negative slope in the change of acoustic velocities as function of pressure is characteristic of glasses with covalent bonds. The followed behavior is in agreement with the negative change in the acoustic longitudinal velocity shown by Zhang et al.,¹⁹ where measurements up to 0.5 GPa were reported. At higher pressures, a sudden increase in sound velocity is observed between 0.4 and 5 GPa, followed by a linear rise at a smaller rate up to the highest applied pressure, of 22 GPa. This last behavior is expected from other bulk MGs.²⁹ Results presented in Fig. 5 show then the presence of a transition from a more covalent phase at low pressure to a metallic one when pressure is increased. Unfortunately more data points would be required to reveal at which pressure the change in slope occurs and whether this change is abrupt or smooth. However, 5 GPa is a higher limit pressure value for the transition, which agrees well with the changes in the static structure factor obtained from XRD and shown in Figs. 1 and 2. The fact that the pressure dependence of the sound velocity changes twice slope between 0 and 25 GPa point to at least three phases of distinct mechanical behaviors displayed by amorphous $\text{Ce}_{70}\text{Al}_{10}\text{Ni}_{10}\text{Cu}_{10}$, in line with the three pressure ranges of different density defined solely from analysis of the XRD data. Upon decrease of pressure, the sound velocity becomes slightly smaller than that obtained in the upload process, thus evidencing again the non-reversible character of the polyamorphic transition.

The sound velocity, v , is related to the longitudinal elastic constant of $\text{Ce}_{70}\text{Al}_{10}\text{Ni}_{10}\text{Cu}_{10}$, C , by the following expression: $C = v^2\rho$, where ρ is the mass density, i.e. inversely proportional to the specific volume. The inset of Fig. 5(b) displays the combination of both static and dynamic effects of the polyamorphic transition by showing the pressure dependence of C relative to its value at ambient pressure, C_0 . Two changes are again observed: A softening of C from 0 to 0.4 GPa is followed by a sudden stiffening of the elastic constant up to 5 GPa, followed then by a linear behavior up to the applied highest pressure, 22 GPa. The three regions displayed by the pressure dependence of C further strengthen the three density domains described in Section III A. Since the sound velocity decreases from compression to decompression, and the specific volume also decreases from one to the other, a partial cancellation of both effects is to be expected for the elastic constant. In agreement with this, no hysteresis can be assigned so far to the elastic constant, within the experimental resolution, although more IXS data upon

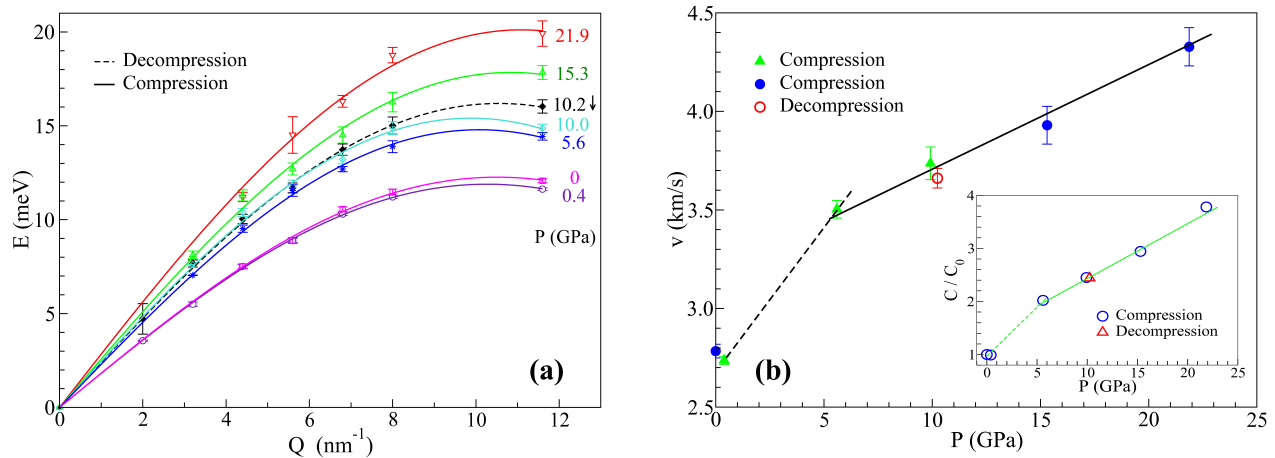


FIG. 5: (a) Dispersion relation of the inelastic excitations obtained from a damped harmonic oscillator model. (b) Sound velocities dependence of hydrostatic pressure. The inset displays the change with pressure of the relative longitudinal elastic constant.

decompression would be required to make a firm statement. The extrapolation of the elastic constant of the high density state to ambient pressure reveals a stiffening of 20% with respect to the low density state, at 0 GPa, as a consequence of the polyamorphic transition.

The IXS data therefore confirm the existence of three different mechanical behaviors of amorphous $\text{Ce}_{70}\text{Al}_{10}\text{Ni}_{10}\text{Cu}_{10}$ in the 0 to 22 GPa pressure range. The negative slope of both longitudinal sound velocity and elastic constant at low pressure corresponds with a softening of the mode energies typical of glasses with covalent bonds. The intermediate pressure range thus correspond to a change from covalent-like to metallic-like bonding behavior in glasses under pressure, which then stabilizes at higher pressures. More IXS pressure points are required to establish the transition between these three regions.

C. Discussion

The combination of both XRD and IXS point out to a gradual non-reversible transition between a low density and a high density state. The origins of this transition can be retraced back to crystalline Cerium, which exhibits a polymorphic transition stemming from the $4f$ electrons strong correlation.^{14,15} Experimentally, the fcc α phase of Ce transforms into a fcc γ phase when temperature is increased and the transformation is linked to a large change in the volume. When pressure is applied at room temperature, the isostructural $\gamma - \alpha$ phase transition is observed at around 0.9 GPa accompanied with a decrease in volume of 15%. This structural behavior has been linked to the electronic behavior of the $4f$ electrons of Ce and pressure induced delocalization was observed. This delocalization has been recently reported to induce strong changes in both phonon dispersions and a strong

electron phonon coupling.³⁰

Unlike crystalline Ce in which the transition occurs sharply, polyamorphic transitions in Ce-based metallic glasses are smooth and continuous over a pressure range and present a hysteresis cycle by decreasing pressure. It is therefore expected that changing the Ce concentration will allow for a detailed study of the interplay between electronic and lattice roles in the polyamorphic transformation.

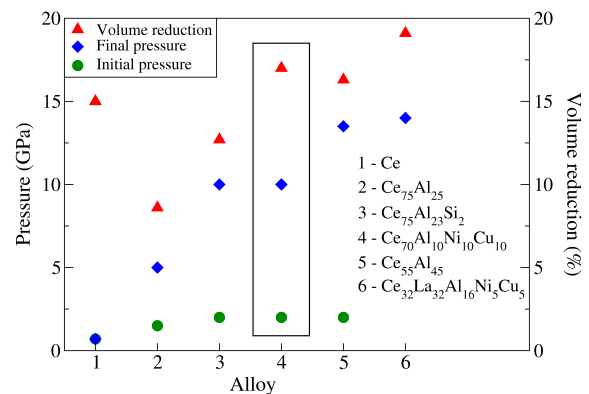


FIG. 6: Pressure range of the polyamorphic transition and volume reduction observed in different Ce-based metallic glasses. Data were taken from Refs. 13,16,31, and 32 except for the $\text{Ce}_{70}\text{Al}_{10}\text{Ni}_{10}\text{Cu}_{10}$ metallic glass.

Figure 6 summarizes the volume reduction estimated and the pressure range at which the transition takes place in different Ce-based alloys including also the results obtained in this work. The value of the starting pressure of the transition for the lowest Ce concentration MG is not reported in the literature. A larger pressure range is observed when Ce concentration decreases, with a saturation for the final pressure at 50% Ce atom concentration. This can be explained by considering the local

environments in each alloy. Crystalline Ce owns a unique and identical structure throughout the material and the transformation occurs at the same time for all atoms. Adding foreign atoms increases the disorder in the alloy and modifies the local environment of Ce. Therefore, a change in the coordination as well as the electronic properties is also observed. In Ce-based metallic glasses, the smallest pressure range and volume collapse for the transformation occurs for $\text{Ce}_{75}\text{Al}_{25}$ metallic glass,¹⁶ which shares the stoichiometric concentration of AlCe_3 intermetallic phase. When a small concentration of aluminum is substituted by a more covalent atom such as silicon, as in $\text{Ce}_{75}\text{Al}_{23}\text{Si}_2$ metallic glass,³¹ the transition pressure is modified displaying a transition pressure range twice as large as for the parent compound. With the incorporation of more foreign atoms and the consequent reduction of Ce concentration in $\text{Ce}_{70}\text{Al}_{10}\text{Ni}_{10}\text{Cu}_{10}$, $\text{Ce}_{55}\text{Al}_{45}$ ¹³ and $\text{Ce}_{32}\text{La}_{32}\text{Al}_{16}\text{Ni}_5\text{Cu}_5$ ³² the alloys transform at different rate and the pressure range of the transformation and the volume reduction increase as the Ce-Ce coordination decreases. Below a certain critical Ce atomic concentration, the $4f$ electron correlation effects are expected to decrease dramatically, and therefore further dilution of Cerium does not alter the final pressure of the transformation. Finally, note that the transformation starts for all reported values around 2 GPa, independently of the Ce concentration, and at pressures relatively close to that of the polymorphic transformation of crystalline Cerium.

We expect that this work will stimulate further IXS investigations on Ce-based MGs under pressure to uncouple electronic and lattice degrees of freedom and achieve a better comprehension of polyamorphic transformations in these alloys. A step further in the investigation of polyamorphic transitions in Ce-based alloys would require to ascertain the specific changes in the electronic structure and bonding driven by Ce $4f$ localization, and can be accessed by inelastic X-ray scattering in the eV energy range, which was not undertaken at this stage. Further information can be obtained by means of X-ray absorption experiments under pressure, which would uncover the local atomic rearrangements taking place at the electronic delocalization and the polyamorphic macroscopic transition.

IV. CONCLUSIONS

We have reported a thorough investigation of the behavior of structural and mechanic properties of $\text{Ce}_{70}\text{Al}_{10}\text{Ni}_{10}\text{Cu}_{10}$ by X-ray diffraction and inelastic X-ray scattering upon application of pressure up to 25 GPa. A low and a high density amorphous phase were found

at different pressure ranges, with an intermediate density region which could be a mixture of both phases between 2 and 10 GPa. Decompression from the high density phase results into a reversible change to the ambient pressure phase, though hysteresis is observed in the static structure factor for the intermediate density region. The XRD results correlate well with changes with pressure in the longitudinal acoustic sound speed and the associated elastic constant as revealed by IXS experiments. The hysteresis in structural changes affects the acoustic sound speed and becomes more apparent in the comparison of acoustic mode energies at high momentum transfers. Both structural and dynamical hysteresis effects seem to cancel each other in the estimate of the longitudinal elastic constant.

The observed polyamorphic transition in $\text{Ce}_{70}\text{Al}_{10}\text{Ni}_{10}\text{Cu}_{10}$ upon application of pressure is attributed to a change in Ce $4f$ electrons from a localized electronic structure to an itinerant one, similarly to the results reported for other Ce-based MGs and for crystalline Ce. The analysis of reported data on similar polyamorphic transitions for other Ce-based amorphous alloys reveals a broadening of the intermediate density region with increasing atomic alloying and reducing Ce content related to higher diversity of local environments in the more complex Ce-based metallic glasses. This broadening seems to saturate upon decrease of Ce concentrations below 55%. The lower limit for the polyamorphic transformation remains nearly unchanged, at 2 GPa, i.e. double the $\gamma - \alpha$ transition in crystalline Cerium, up to a concentration of 55% atomic Cerium. Further IXS experiments on intermediate Ce-content amorphous alloys are required to fully uncouple the role of $4f$ Ce electrons from lattice degrees of freedom in the polyamorphic transformation.

Acknowledgments

We acknowledge the European Synchrotron Radiation Facility for provision of synchrotron radiation facilities under proposals CGR-16-01-726 and HD-349 and we would like to thank A. Labrador for assistance in using beamlines BM16. EP, DC and JS thank the financial support of CICYT grant MAT2010-14907 and Generalitat de Catalunya grant 2009SGR1225. PB thanks the financial support of Generalitat de Catalunya grant 2009SGR1251. MJD and AHR thanks the support of Conacyt, México, through projects PPPROALMEX-DAAD-Conacyt and 152153. WHW thanks the financial support from NSF of China (50921091 and 50731008) and MOST973 of China (2007CB613904 and 2010CB731603).

¹ O. Mishima, L. D. Calvert, and E. Whalley, *Nature* **314**, 76 (1985).

² Y. Katayama, T. Mizutani, W. Utsumi, O. Shimomura, M. Yamakata, and K. Funakoshi, *Nature* **403**, 170 (2000).

- ³ R. Winter, C. Szornel, W. C. Pilgrim, W. S. Howells, P. A. Egelstaff, and T. Bodensteiner, *J. Phys. Condens. Matter* **2**, 8427 (1990).
- ⁴ T. Morishita, *Phys. Rev. Lett.* **93**, 055503 (2004).
- ⁵ S. K. Deb, M. Wilding, M. Somayazulu, and P. F. McMillan, *Nature* **414**, 528 (2001).
- ⁶ S. Sastry and C. A. Angell, *Nature Mater.* **2**, 739 (2003).
- ⁷ M. C. Wilding and P. F. McMillan, *J. Non-Cryst. Solids* **293**, 357 (2001).
- ⁸ P. F. McMillan and M. C. Wilding, *J. Non-Cryst. Solids* **354**, 1015 (2008).
- ⁹ C. Meade, R. J. Hemley, and H. K. Mao, *Phys. Rev. Lett.* **69**, 1387 (1992).
- ¹⁰ L. Huang, L. Duffrene, and J. Kieffer, *J. Non-Cryst. Solids* **349**, 1 (2004).
- ¹¹ S. Sen, S. Gaudio, B. G. Aitken, and C. E. Leshner, *Phys. Rev. Lett.* **97**, 025504 (2006).
- ¹² M. F. Ashby and A. L. Greer, *Scr. Mater.* **54**, 321 (2006).
- ¹³ H. W. Sheng, H. Z. Liu, Y. Q. Cheng, J. Wen, P. L. Lee, W. K. Luo, S. D. Shastri, and E. Ma, *Nature Mater.* **6**, 192 (2007).
- ¹⁴ P. Soderlind, *Adv. Phys.* **47**, 959 (1998).
- ¹⁵ A. B. Shick, W. E. Pickett, and A. I. Liechtenstein, *J. Electron Spectrosc. Relat. Phenom.* **114**, 753 (Mar. 2001).
- ¹⁶ Q. S. Zeng, Y. Ding, W. L. Mao, W. Yang, S. V. Sinogeikin, J. Shu, H. K. Mao, and J. Z. Jiang, *Phys. Rev. Lett.* **104**, 105702 (2010).
- ¹⁷ Q. S. Zeng, V. V. Struzhkin, Y. Z. Fang, C. X. Gao, H. B. Luo, X. D. Wang, C. Lathe, W. L. Mao, F. M. Wu, H.-K. Mao, and J. Z. Jiang, *Phys. Rev. B* **82**, 054111 (2010).
- ¹⁸ B. Zhang, R. J. Wang, D. Q. Zhao, M. X. Pan, and W. H. Wang, *Phys. Rev. B* **70**, 224208 (2004).
- ¹⁹ B. Zhang, R. J. Wang, and W. H. Wang, *Phys. Rev. B* **72**, 104205 (2005).
- ²⁰ H. K. Mao and P. M. Bell, *Science* **191**, 851 (1976).
- ²¹ Z. Liu, Q. Cui, and G. Zou, *Phys. Lett. A* **143**, 79 (1990).
- ²² F. D. Murnaghan, *Proc. Natl. Acad. Sci. U.S.A* **30**, 244 (1944).
- ²³ A. Svane, W. M. Temmerman, Z. Szotek, J. Lgsgaard, and H. Winter, *Int. J. Quantum Chem.* **77**, 799 (2000).
- ²⁴ W. E. Pickett, *Physica* **111B**, 1(1981).
- ²⁵ G. Rout, M. S. Ojha, and S. N. Behera, *Physica B* **367**, 101 (2005).
- ²⁶ T. Scopigno, J. B. Suck, R. Angelini, F. Albergamo, and G. Ruocco, *Phys. Rev. Lett.* **96**, 135501 (2006).
- ²⁷ B. Rufflé, G. Guimbretière, E. Courtens, R. Vacher, and G. Monaco, *Phys. Rev. Lett.* **96**, 045502 (2006).
- ²⁸ G. Monaco, *C. R. Phys.* **9**, 608 (2008).
- ²⁹ W. H. Wang, F. Y. Li, M. X. Pan, D. Q. Zhao, and R. J. Wang, *Acta Mater.* **52**, 715 (2004).
- ³⁰ Michael Krisch, D. L. Farber, R. Xu, Daniele Antonangeli, C. M. Aracne, Alexandre Beraud, Tai-Chang Chiang, J. Zarestky, Duck Young Kim, and Eyvaz I. Isaev, and Rajeev Ahuja, Börje Johansson, *Proc. Natl. Acad. Sci. U.S.A* **108**, 9342 (2011).
- ³¹ Q. S. Zeng, Y. Z. Fang, H. B. Lou, Y. Gong, X. D. Wang, K. Yang, A. G. Li, S. Yan, C. Lathe, F. M. Wu, X. H. Yu, and J. Z. Jiang, *J. Phys. Condens. Matter* **22**, 375404 (2010).
- ³² Q. S. Zeng, Y. C. Li, C. M. Feng, P. Liermann, M. Somayazulu, G. Y. Shen, H. K. Mao, R. Yang, J. Liu, T. D. Hu, and J. Z. Jiang, *Proc. Natl. Acad. Sci. U.S.A* **104**, 13565 (2007).